ACS APPLIED ENERGY MATERIALS

www.acsaem.org Article

Ionic Conductivity, Na Plating–Stripping, and Battery Performance of Solid Polymer Na Ion Electrolyte Based on Poly(vinylidene fluoride) and Poly(vinyl pyrrolidone)

Afshana Afroj Bristi, Alfred Junio Samson, Abinaya Sivakumaran, Shantel Butler, and Venkataraman Thangadurai*

Cite This: *ACS Appl. Energy Mater.* 2022, 5, 8812–8822 Read Online

ACCESS | Metrics & More | Article Recommendations | Supporting Information

ABSTRACT: Solid-state sodium-ion batteries (ss-SIBs) are a promising alternative to commercially available lithium-ion batteries for next-generation energy storage applications due to the abundance and cost-effectiveness of sodium over lithium. Herein, using a facile solution casting process, a high sodium-ion conductive, filler-less composite solid polymer electrolyte (SPE) film based on poly(vinylidene fluoride) polymer, poly(vinyl pyrrolidone) (PVP) binder, and $NaPF_6$ salt for ss-SIB has been successfully fabricated. Total conductivities of 8.51×10^{-4} and 8.36×10^{-3} S cm^{-1} at 23 and 83 °C, respectively, were observed from the SPE. A hybrid symmetric half-cell assembly using Na electrode and 1 M $NaClO_4$ in ethylene carbonate (EC) and propylene carbonate (PC) (EC/PC = 1:1 wt %) electrolyte showed excellent Na plating–stripping performance at 10 mA cm^{-2} at 23 °C. The study showed that PVP binder played an important role in achieving good Na ion conductivity and excellent Na plating–stripping performance, highlighting the applicability of the as-prepared SPE in next-generation high-power rechargeable SIBs. A full cell with an SPE, a Na anode, and a $Na_3V_2(PO_4)_3$ cathode showed a discharge capacity of 93.2 mAh g^{-1} at 0.1 C with 86% capacity retention and 99.68% Coulombic efficiency for 100 cycles.

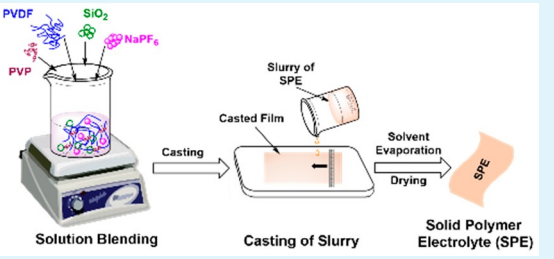

KEYWORDS: *solid-state sodium-ion battery, solid polymer electrolyte, plating–stripping, ionic conductivity, symmetric Na cell*

INTRODUCTION

Next-generation energy storage technologies require excellent safety, low-cost materials, and high energy density.[1−3] Solid-state sodium-ion batteries (ss-SIBs) are believed to be a promising alternative to commercially available lithium-ion batteries (LIBs) due to low materials costs, the abundance and availability of sodium over lithium, and greatly improved safety.[4,5] Commercially available organic liquid or gel electrolyte-based LIBs exhibit low thermal stability, high flammability, high volatility, and leakage of toxic organic solvents.[6,7] In the liquid-based LIBs and SIBs, premature battery failure may take place when the electrolyte continuously reacts with the electrode and causes dendrite-induced internal short circuits.[8] In contrast, solid-state electrolytes (SSEs) could prevent this short circuit because they have the ability to physically block metal dendrites.[9] Two types of SSEs include inorganic (ceramic and glass sulfides) and organic polymers, both of which are also called solid polymer electrolytes (SPEs).[10−14] Solid electrolytes exhibit higher ion transference number than liquid electrolytes. However, poor interfacial properties and relatively low ionic conductivity are the main drawbacks of SSEs.[15,16] Several strategies have been adopted to overcome these existing issues in both ceramic electrolytes and SPEs.[17−19] Artificial solid electrolyte interphase (SEI) layer assembly,[20] hybrid electrolytes,[21,22] and porous solids[23] are being considered as promising approaches to improve interfacial contact between the solid electrolyte and the electrodes.

Incorporating SPEs into ss-SIBs has been one of the most attractive strategies because of the easy processability and low cost of SPEs.[24,16] The Na ion conductivities of solid-state polymer electrolytes are typically between 10^{-6} and 10^{-5} S cm^{-1} at room temperature, significantly lower than those of liquid electrolytes.[25,26] The degree of crystallinity of polymer materials, coupling between ionic motion and segmental motion, and the local relaxation of the polymer chain are assumed to be the main reasons for low ionic conductivity.[27] Different approaches, including modification of polymer materials, adding plasticizers (e.g., dimethylformamide (DMF) solvent), and adding nanofillers (e.g., SiO_2, Al_2O_3) have been considered over the years to improve the room temperature conductivity of SPEs.[28,29] Poly(ethylene oxide) (PEO) and poly(vinylidene fluoride)

Received: April 28, 2022
Accepted: June 14, 2022
Published: June 28, 2022

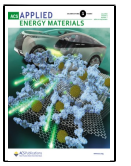

https://doi.org/10.1021/acsaem.2c01296
ACS Appl. Energy Mater. 2022, 5, 8812–8822

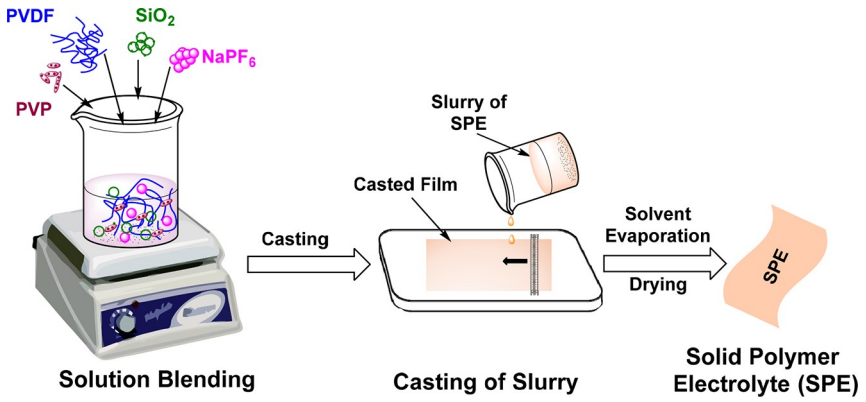

Figure 1. Fabrication of SPE by solution blending technique.

(PVDF) matrices mixed with Na salt (e.g., $NaPF_6$) are widely studied for use in ss-SIBs.[30,18] PVDF-based electrolytes have better mechanical strength and higher melting points than PEO-based electrolytes.[31,32] Decreasing the thickness of SPEs helps to reach higher energy densities. Maintaining good mechanical properties[33] and thickness of SPEs could be achieved by using conventional doctor-blade or roll-to-roll coating processes.[34]

Several studies that incorporated nano- or mixed-sized fillers in PVDF-based SPEs found that the ionic conductivity and mechanical properties of the SPEs were influenced significantly. Sun et al.[35] demonstrated that 10 wt % mixed-sized Nb/Al doped $Li_7La_3Zr_2O_{12}$ (LLZO)−PVDF−$LiClO_4$-based composite polymer electrolyte exhibited a maximum conductivity of 2.6×10^{-4} S cm^{-1}, an order of magnitude higher than that with nano- or micrometer-sized LLZO particles as fillers. Hema et al.[36] reported that adding 8 mol % inorganic nanofiller (e.g., SiO_2 and TiO_2) into a poly(vinyl alcohol) (PVA)−PVDF−$LiCF_3SO_3$-based nanocomposite polymer electrolyte resulted in enhanced ionic conductivity up to 3.7×10^{-3} S cm^{-1} compared with electrolyte without the nanofiller. Furthermore, different research findings explained that salt concentration and structural impact on ionic transport are also important in composite SPE systems.[37,38] Over the past decade, linear, branched, and three-dimensional (3D)-structured functional polymer binding materials have attracted significant attention in developing solid electrolyte interphase layers, mechanical strength, and stable cycling performance of Si-based anodes.[39,40] Zheng et al.[41] demonstrated a functionalized poly(vinyl pyrrolidone) (PVP) doped polyaniline linear binder that enhanced conductivity, cycling, and electrochemical stability of Si anodes for LIBs.

Here, we have fabricated a novel PVDF, PVP polymer binder, and $NaPF_6$ salt based SPE by a facile solution casting process. The effect of different $NaPF_6$ salt concentrations and the impact of SiO_2 nanofiller and PVP binder on a PVDF-based SPE for SIBs were investigated. Optimized filler-free and PVP binder-assisted SPEs showed high Na ion conductivity, excellent Na plating−stripping performance, and stable battery cycling with Na anode and $Na_3V_2(PO_4)_3$ (NVP) cathode.

EXPERIMENTAL SECTION

Synthesis of Composite Solid Polymer Electrolyte (SPE). PVDF and $NaPF_6$ salt were obtained from Alfa Aesar, and PVP (M_W = 40000) and DMF solvent were purchased from Sigma-Aldrich. The solution-casting technique is shown schematically in Figure 1.

Six SPE films were prepared to study the effect of the amount of salt, filler, and binder on the Na ion conductivity, compatibility with Na anode, and physical properties (Table 1). Three SPEs (SPE-1, SPE-2, and SPE-3) with varying molar ratios of PVDF and $NaPF_6$ salt (PVDF/$NaPF_6$ = 4:1, 9:1, 17:1) were prepared to study the effect of the amount of salt. The samples have no SiO_2 nanofiller and contain the same amount of PVP binder (11 wt % with PVDF). First, different ratios of PVDF and $NaPF_6$ were dissolved in dimethylformamide (DMF) (6 times the total amount of PVDF and $NaPF_6$) at 23 °C. After fully mixing the PVDF and Na salt, PVP was added into the solution and stirred for 1 h to produce the SPE slurries. Afterward, the slurry was cast onto a glass plate with the aid of a doctor blade and dried for 24 h in vacuum oven at 22 °C. The films (thickness ∼0.02 cm) of composite SPEs obtained after drying were cut into circular discs for further electrochemical and physicochemical measurements. The image of one of the circular shaped SPEs (SPE-2) is shown in Figure S1a. A sample with SiO_2 (size 5−15 nm; 2 wt % of PVDF; obtained from Sigma-Aldrich; SPE-4) and a sample based on SiO_2 and PVP (SPE-5) were fabricated to investigate the impact of nanofiller and the combined effect of SiO_2 and PVP on the composite SPE system. Finally, a sample (SPE-6) without SiO_2 and PVP with 9:1 ratio of PVDF and $NaPF_6$ was prepared and used to compare and identify the impact of PVP binder on ionic conductivity and compatibility with Na anode.

Table 1. Chemical Compositions and Ionic Conductivity at Room Temperature (21−23 °C) of the SPEs[a]

solid polymer electrolytes	chemical composition	conductivity (S cm^{-1})
SPE-1	PVDF/$NaPF_6$ (4:1) + PVP (11 wt % of PVDF)	8.47×10^{-4}
SPE-2	PVDF/$NaPF_6$ (9:1) + PVP (11 wt % of PVDF)	8.51×10^{-4}
SPE-3	PVDF/$NaPF_6$ (17:1) + PVP (11 wt % of PVDF)	1.79×10^{-5}
SPE-4	PVDF/$NaPF_6$ (9:1) + SiO_2 (2 wt % of PVDF)	2.28×10^{-4}
SPE-5	PVDF/$NaPF_6$ (9:1) + PVP (11 wt % of PVDF) + SiO_2 (2 wt % of PVDF)	1.10×10^{-4}
SPE-6	PVDF/$NaPF_6$ (9:1)	2.10×10^{-6}

[a]PVDF and $NaPF_6$ compositions are expressed as molar ratios.

Material Characterization. The phases in the SPE were determined by X-ray diffraction (XRD) using a Bruker D8 Advance diffractometer (Cu Kα, 40 kV, 40 mA). The micromorphology of the SPEs was analyzed by field-emission scanning electron microscopy (FE-SEM, Zeiss Sigma VP). The elemental composition of the composite electrolyte was studied by energy-dispersive X-ray spectroscopy (EDX; OXFORD ISI 300 EDAX attached to the Zeiss Sigma VP FE-SEM). The SPEs were characterized by Fourier transform infrared (FTIR) spectroscopy (Thermo-Nicolet Nexus 470) to identify the influence of chemical functional groups of the precursors in the composite films. Raman spectral data were collected using a Bruker RAM II with a 1064 nm wavelength laser. Thermogravimetric analysis

https://doi.org/10.1021/acsaem.2c01296
ACS Appl. Energy Mater. 2022, 5, 8812−8822

(TGA) was performed using a METTLER TOLEDO thermal system TGA/DSC1 (HT 1600). The diameter and thickness of the SPEs were approximately 1.0 and 0.02 cm, respectively.

Electrochemical Measurements. The impedance spectra of the SPEs were obtained using a Princeton (Versa STAT 3) potentiostat/galvanostat/frequency analyzer in the frequency range of 1 MHz to 0.1 Hz. A split cell (MTI Corp.) was used to simply sandwich the SPEs between two stainless-steel blocking type electrodes where no liquid electrolyte was used in this electrochemical impedance spectra (EIS) measurement setup. The ionic conductivity of the SPEs was estimated using the equation

$$\sigma = l/(AR) \quad (1)$$

where l is the thickness, A is the area, and R is the measured resistance of the electrolyte.

Na plating−stripping experiments were performed with three different symmetric cell configurations (Na-foil|SPE|Na-foil, Na foil|liquid|Na foil, and Na-liquid|SPE|liquid-Na) to investigate the compatibility and stability of the SPE with Na metal anode. A typical hybrid symmetric cell assembly (Na foil + 20 μL of 1 M $NaClO_4$ in ethylene carbonate (EC)/propylene carbonate (PC) (1:1) + carbon-cloth|SPE-2|carbon-cloth + 20 μL of 1 M $NaClO_4$ in EC/PC (1:1)|Na foil) inside a CR2032 coin cell case is shown in Figure 2. Carbon cloths

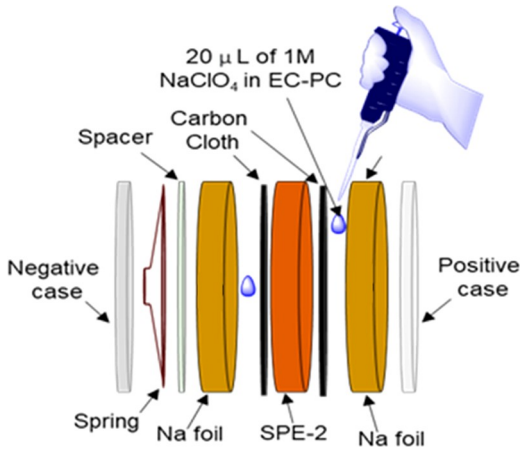

Figure 2. Symmetrical Na cell set up for galvanostatic cycling interfacial resistance. The 1 M liquid electrolyte was prepared by dissolving $NaClO_4$ salt into a mixture of PC (Sigma-Aldrich) and EC (DodoChem) organic solvents (PC/EC = 1:1 by weight).

(0.1 mm, Fuel Cell Store) were placed between the Na anode and the SPE to minimize the possible side reactions' effect in the Na/SPE interface that could be attributed to the polarization of active Na metal anode by the hydrophilic nature (containing C═O and C−N moieties) of PVP polymer binder in the presence of trapped DMF solvent in the PVDF host polymer matrix. Liquid electrolyte (20 μL cm^{-2} of 1 M $NaClO_4$) was added between the interfaces of Na electrode and carbon cloth to decrease the interfacial resistance. The 1 M liquid electrolyte was prepared by dissolving $NaClO_4$ salt into a mixture of PC (Sigma-Aldrich) and EC (obtained from DodoChem) organic solvents (PC/EC = 1:1 by weight).

Electrode Fabrication and Full-Cell Assembly. The $Na_3V_2(PO_4)_3$ (NVP) cathode was prepared by mixing the NVP powder (MTI corporation) with super P conductive carbon and PVDF binder at a weight ratio of 8:1:1 in *N*-methyl pyrrolidone (NMP) solvent to form a homogeneous slurry. The slurry was uniformly coated on an Al foil using a doctor blade and dried in a vacuum oven at 60 °C overnight. The cathode-coated Al foil was cut into a 1 cm diameter circular disc electrode (area of 0.79 cm^2). The calculated average mass loading of the active material was 3.01 mg cm^{-2}. Among the six fabricated SPEs, SPE-2, with the highest ionic conductivity, was considered for battery performance demonstration and for further characterization. A CR2032 coin cell was fabricated using the as-prepared cathode disc, SPE-2, 20 μL of 1 M $NaClO_4$ EC/PC (1:1) liquid electrolyte, carbon cloth, and Na metal anode (Na foil + 20 μL of 1 M $NaClO_4$ in EC/PC (1:1) + carbon-cloth|SPE-2|20 μL of 1 M $NaClO_4$ in EC/PC (1:1)|NVP). Carbon cloth was used to minimize the side reaction between the anode and SPE-2. Also, 20 μL of 1 M $NaClO_4$ EC/PC (1:1) liquid electrolyte was used to reduce the interfacial resistance.

RESULTS AND DISCUSSION

Morphological Analysis of SPEs. The SEM images of the SPEs are shown in Figure 3a−g. Figure 3a−c shows the SEM images of SPEs with varying amounts of $NaPF_6$ salt (SPE-1, SPE-2, and SPE-3, respectively) under the same magnification. From Figure 3a−c and the magnified images in Figure S1b,c,d, it can be concluded that the sample with the highest amount of $NaPF_6$ (SPE-1) exhibited the smoothest surface among the samples. The surface SEM images (Figure 3b and Figure S1c) of SPE-2 indicate the existence of some degree of porosity on its surface. In addition, a magnified surface image of SPE-2 (Figure 3f) exhibited a porous surface. The SEM images (Figure 3d,e) of SiO_2-containing SPE-4 and SPE-5 exhibited comparatively higher surface roughness and apparently no surface porosity compared with the samples without SiO_2 (SPE-1, SPE-2, and SPE-3). This feature of SPE-4 and SPE-5 can be attributed to the presence of SiO_2, which fills the nanogaps of the surfaces of SPEs. SiO_2 coagulates due to its lower affinity with the PVDF host polymer in the presence of a PVP binder.[42−44] From the cross-sectional view of SPE-2 (Figure 3g), it may be claimed that the polymer host and Na-salt (PVDF/$NaPF_6$ = 9:1) in the SPE-2 provide interconnected porous structure. In the hybrid symmetric cell setup (Figure 2), the liquid electrolyte uptake took place easily and expanded the ion transfer channels owing to this interconnected porous structure, resulting in less impedance of Na ion diffusion. Further, the component elements of PVDF, PVP, and $NaPF_6$ salt in the composite SPE-2 film were detected by EDX (Figure 3h), as expected.

Electrochemical Performance of SPEs. The electrical characterization of the as-prepared SPEs was conducted using AC impedance spectroscopy. The room temperature EIS profiles of the SPEs are presented in Figure 4 as Nyquist plots. Only a tail at the high frequency side was observed for all samples except SPE-3. A semicircle at the high frequency side and a tail at the low frequency side were observed for SPE-3. The tail indicates the blocking nature of the stainless steel (SS) electrode against Na ions.[45] For all SPEs, the starting point of the tail is considered as the total electrolyte resistance for the conductivity (σ) calculation using eq 1. The calculated ionic conductivities of SPEs are summarized in Table 1. The ionic conductivity of the SPEs at higher temperatures were determined and shown in the Supporting Information (SPE-1, Figure S2 and Table S2; SPE-2, Figure 5a and Table S3; SPE-3, Figure S3 and Table S4). SPE-2 showed the highest ionic conductivity of 8.51×10^{-4} S cm^{-1} at 23 °C and 8.36×10^{-3} S cm^{-1} at 83 °C. The amount of $NaPF_6$ was at the optimum for SPE-2, thus it showed higher ionic conductivity than SPE-1 and SPE-3. Low Na ion concentration in the SPE-3 provided a low charge carrier number in the composite electrolyte system, resulting in the lowest conductivity of 1.79×10^{-5} S cm^{-1}. On the other hand, the high Na ion concentration in SPE-1 most likely resulted in the interaction of ions with each other, resulting in lower conductivity than SPE-2. The presence of nanofiller SiO_2 (2 wt % of PVDF) in the SPE-4 and SPE-5 decreased the Na ion conductivity. Because the polarity of the O atom (Lewis

https://doi.org/10.1021/acsaem.2c01296
ACS Appl. Energy Mater. 2022, 5, 8812−8822

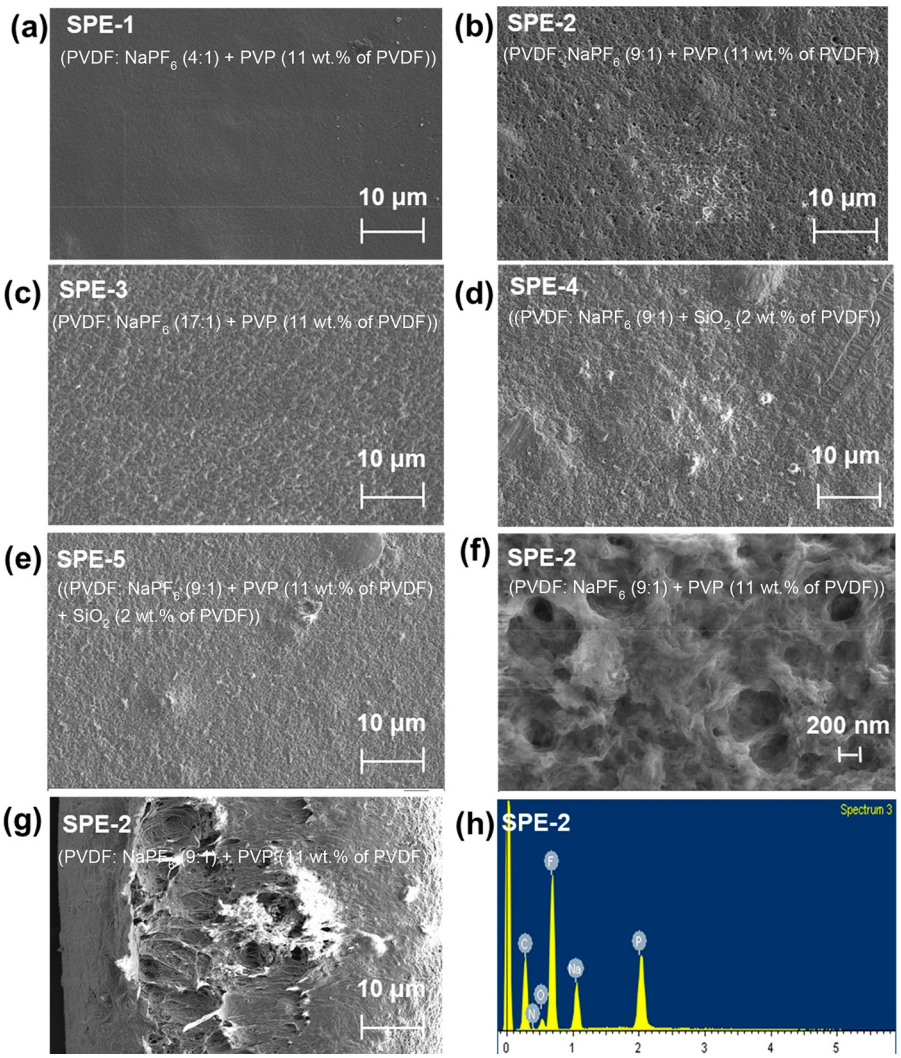

Figure 3. Surface SEM images of (a) SPE-1, (b) SPE-2, (c) SPE-3, (d) SPE-4, (e) SPE-5, and (f) SPE-2 (magnified). (g) Cross-sectional SEM and (h) EDX spectrum of SPE-2.

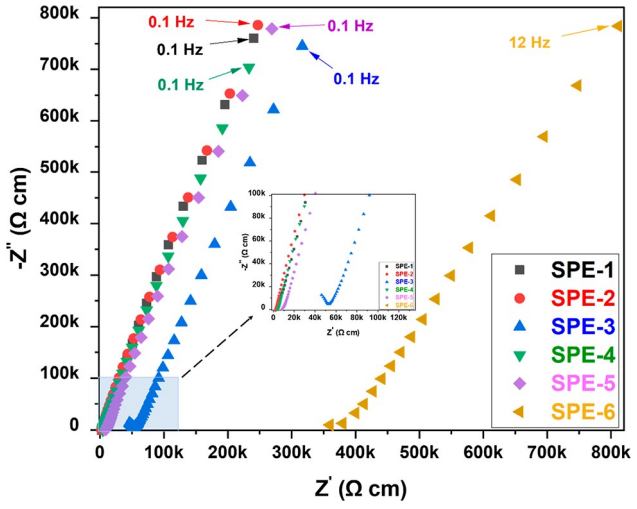

Figure 4. Electrochemical impedance spectra (EIS) of SPEs at RT (21−23 °C).

basic site) in a PVP molecule is higher than that of O atom in SiO_2,[46,47] PVP could provide stronger interaction than SiO_2 to dissociate the ion pair of the $NaPF_6$ salt, bringing extra charge carriers for enhanced conductivity. However, the SiO_2 and PVP-containing SPE-5 showed lower ionic conductivity than the binder-less SPE-4. Among the literature reported PVDF-based SPEs, the ionic conductivity of SPE-2 at room temperature was one of the highest reported values, as shown in Table 2.[18,48,49]

The low conductivity may be explained by the competing interaction of PVP and SiO_2 toward Na-salt, leading to less ion dissociation in the SPE-5 system. A filler and binder-less sample (SPE-6; PVDF/$NaPF_6$ = 9:1) was prepared to investigate the effect of PVP binder on ionic conductivity. The sample exhibited an ionic conductivity of 2.1×10^{-6} S cm^{-1} at 23 °C, significantly lower than that of PVP-doped SPE-2. This result implies that PVP played a crucial role in improving the ionic conductivity of the PVDF and $NaPF_6$-based SPE systems. The conductivities of SPE-2 at different temperatures (23 to 83 °C) are shown in Figure 5a,b. SPE-2 showed the highest conductivity ($\sigma = 8.36 \times 10^{-3}$ S cm^{-1}) at 83 °C. The activation energy for ionic conductivity was estimated using the Arrhenius equation:

$$\sigma T = A \exp\left(-\frac{E_a}{kT}\right) \quad (2)$$

where A is the pre-exponential factor, E_a is the activation energy, T is the temperature, and k is the Boltzmann constant ($1.38 \times$

https://doi.org/10.1021/acsaem.2c01296
ACS Appl. Energy Mater. 2022, 5, 8812−8822

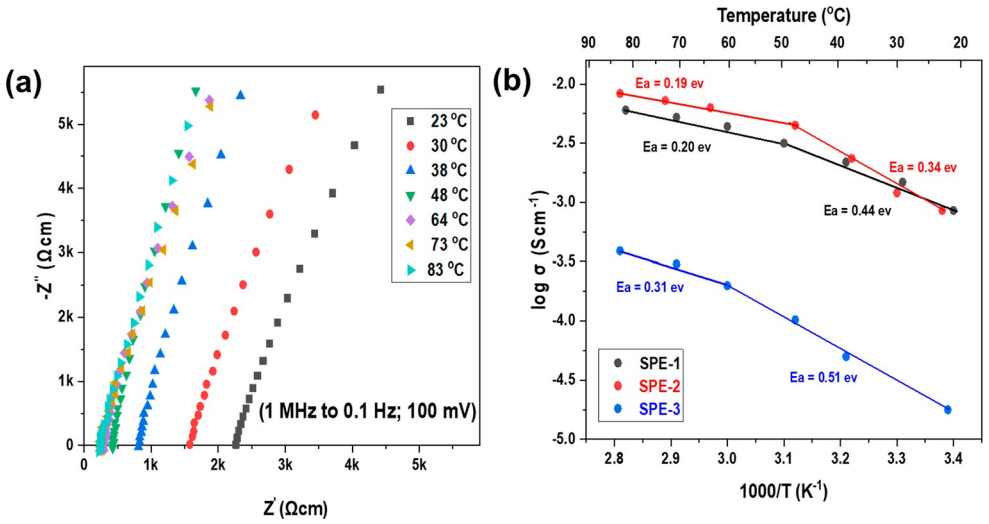

Figure 5. (a) EIS spectra of SPE-2 at different temperatures; (b) Arrhenius plots of SPE-1, SPE-2, and SPE-3.

Table 2. Comparison of the Ionic Conductivity with Reported Literature[18,48,49]

electrolyte	ionic conductivity (S cm^{-1})	temp	ref
PVDF−HFP−LiTFSI	1.9×10^{-4}	RT	48
PVDF−SiO_2−$NaCF_3SO_3$	6×10^{-5}	25 °C	18
PVDF−LiTFSI−LiF−LLBZTO	3.4×10^{-4}	20 °C	49
PVDF−PVP−$NaPF_6$	8.51×10^{-4}	23 °C	present work
PVDF−PVP−$NaPF_6$	8.36×10^{-3}	83 °C	present work

10^{-23} J K^{-1}). The polymeric chain expansion increases with increasing temperature, facilitating free volume expansion inside the polymer matrix. The produced free volume promotes the segmental motion of the polymer, increasing the ionic conductivity as found in SPE-1, SPE-2, and SPE-3.[50] The differences may be due to the dissociation of the salt and amount of free charge carriers in the polymer. In SPE-1, the incomplete dissociation of the high salt content may have decreased the ionic conductivity. On the other hand, the low amount of Na salt in SPE-3 led to a decreased ionic conductivity because of few free charge carriers. The activation energy (E_a) of SPE-1, SPE-2, and SPE-3 has been analyzed from the Arrhenius relationship plots and presented in Figure 5b. All the SPEs showed a nonlinear Arrhenius plot relationship. This type of nonlinear Arrhenius behavior indicates that segmental relaxation of polymer matrices and the ionic motion are connected.[49] SPE-2 exhibited lower activation energy than SPE-1 and SPE-3. The difference may be attributed to the more facile ion hoping possibility in SPE-2 than in SPE-1 and SPE-3 through the amorphous PVDF in the presence of $NaPF_6$ salt. For SPE-2, the activation energy in the high-temperature region (47.5−83 °C) was 0.19 and that in the low-temperature region (23−47.5 °C) was 0.34 eV. The low E_a value (0.19 eV) of SPE-2 suggests that Na ions easily diffused in this composite system. The conductivity and activation energies of PVDF-based SPEs from the literature are summarized, along with the present results, in Table 3.[18,35,49,51,52]

Characterization of the Optimized Solid Polymer Electrolyte (SPE-2). Figure 6 shows the XRD patterns of PVDF, PVDF−$NaPF_6$, PVP, and SPE-2. The XRD pattern of

Table 3. Conductivity, Activation Energy, and Synthesis Conditions of PVDF-Based SPEs Reported in the Literature[18,35,49,51,52]

σ of PVDF based SPEs (S cm^{-1})	E_a (eV)	synthesis conditions	ref
1.00×10^{-4} (25 °C)	0.39	modified sol−gel method (80 °C, 12 h)	35
8.90×10^{-5} (90 °C)	0.47	solution-blending and ball-mill (RT, 48 h)	49
2.93×10^{-4} (90 °C)	0.33	solvent casting (RT, 10 h)	51
6.48×10^{-7} (30 °C)	0.33	solution-blending (50 °C, 3 h)	52
2.10×10^{-6} (25 °C)	0.33	solution-blending and ball-mill (RT, 24 h)	18
8.51×10^{-4} (23 °C)	0.34	solution-blending (RT, 24 h)	present work
8.36×10^{-3} (83 °C)	0.19	solution-blending (RT, 24 h)	present work

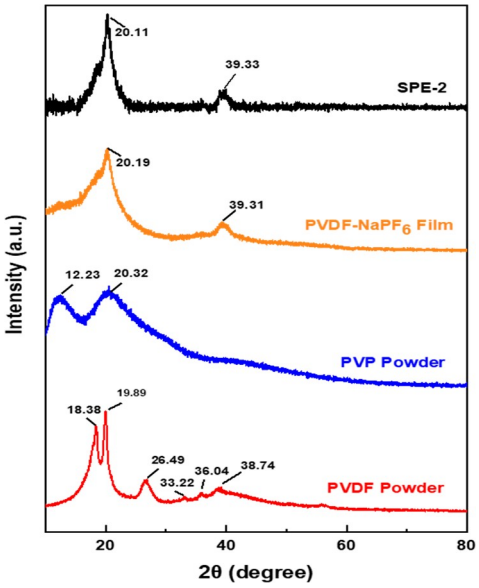

Figure 6. XRD patterns of the PVDF and PVP powders, PVDF−$NaPF_6$ film, and SPE-2.

the PVDF powder displayed two intense peaks at 2θ values of 19.89° and 18.38°, which are assigned to the 110 and 020 planes,

https://doi.org/10.1021/acsaem.2c01296
ACS Appl. Energy Mater. 2022, 5, 8812−8822

respectively. The peak at 26.49° (021) confirmed that the PVDF used in this work was α-phase.[53−55] Two weak peaks at 33.22° and 36.04° correspond to 130 and 002 planes, respectively, for the monoclinic α-phase.[55−57] Another broad peak at 38.74° confirmed the γ-phase of the PVDF.[57,53,58] The two broad peaks at around 12.23° and 20.32° for the PVP indicate the amorphous nature of PVP.[59] The addition of $NaPF_6$ salt into the PVDF broadened the α-phase peak. The change could be attributed to the shift from α- to β-phase. The γ-phase of the PVDF remained the same. In the PVDF−$NaPF_6$ complex, lack of peaks from $NaPF_6$ suggests that the salt was completely dissolved in the PVDF. The XRD pattern of SPE-2 showed less crystallinity. The absence of peaks attributable to Na salt and PVP in SPE-2 indicated that the salt and PVP were completely dissolved.

The FTIR spectral measurement of SPE-2 is summarized in Figure 7. The PVDF powder exhibited characteristic vibrational

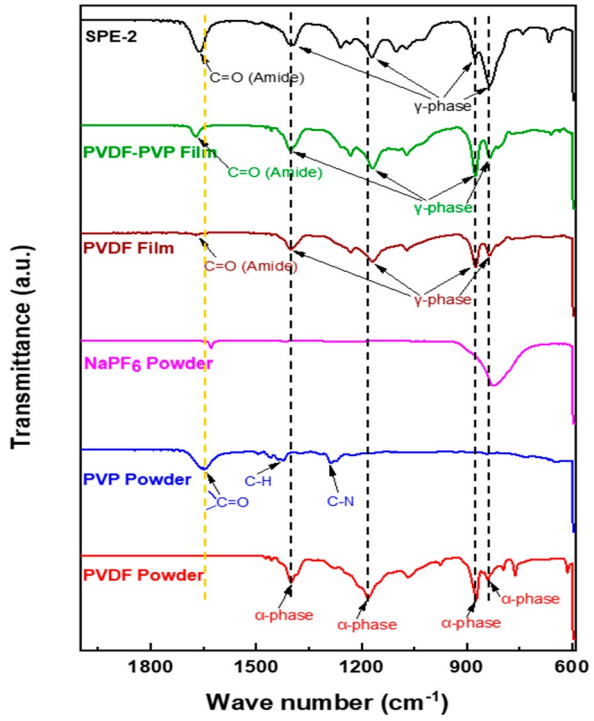

Figure 7. FTIR spectrum of PVDF, PVP, and $NaPF_6$ powders, PVDF and PVDF−PVP films, and SPE-2.

peaks at 613, 763, 796, 840, 873, 950, 973, 1068, 1182, 1207, 1276, and 1400 cm^{-1} and shoulder peaks at 1457 and 1473 cm^{-1}, all attributed to the α-phase of PVDF polymer.[53,58,60] The PVDF film showed characteristic peaks at 809, 836, 875, 1074, 1164, 1232, and 1400 cm^{-1} (Table S1)[58,60] associated with the γ-phase of the PVDF film. The PVDF−PVP complex and SPE-2 exhibited all the peaks associated with the γ-phase of PVDF.[60] Compared to the α-phase, the β- and γ-phases of PVDF are more polar in nature.[18] The polar nature of the polymer helped to enhance the ionic conductivity by reducing the crystallinity of the polymer. Thus, the β- and γ-phases showed better electroactive properties than the α-phase.[61,53] SPE-2 and the PVDF−PVP and PVDF films contained an additional peak at around 1670 cm^{-1}, attributable to the amide group of the DMF solvent trapped in the polymer matrix.[18] The FTIR spectral profile of PVP displayed characteristics peaks at 1650, 1458, and 1288 cm^{-1} that could be attributed to C═O stretching, C−H bending, and C−N stretching, respectively. The presence of C−N stretching was found for the peak at 1371 cm^{-1}. Also, $NaPF_6$ displayed a characteristic hexafluorophosphate stretch at 837 cm^{-1}.

In the Raman spectral profile (Figure 8), characteristic peaks of α-PVDF at 607 and 795 cm^{-1} were observed for the PVDF

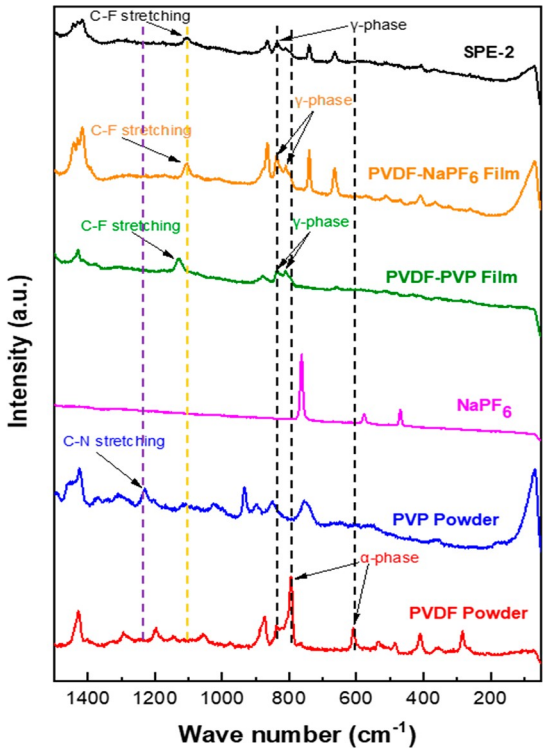

Figure 8. Raman profiles of PVDF and PVP powders, $NaPF_6$ salt, and PVDF−PVP, PVDF−$NaPF_6$, and SPE-2 films.

powder sample, which were due to CF_2 wagging and stretching vibrations, respectively. Two distinct peaks at 796 and 834 cm^{-1} could be attributed to the γ-phase of the PVDF powder.[58] These characteristic γ-phase peaks were found in the Raman profiles of PVDF−PVP, PVDF−$NaPF_6$, and SPE-2 films. The peaks explain the α-phase transition of PVDF to γ-phase and strongly support the FTIR analysis. The Raman spectrum of the $NaPF_6$ salt showed three prominent characteristic peaks at 764, 574, and 467 cm^{-1}.[62,63] After the reaction of pure PVDF with PVP and $NaPF_6$ (Raman profile of SPE-2), the C−F stretching peak of pure PVDF weakened and shifted to the lower frequency region at 1103 cm^{-1}. Similar changes were observed for the PVDF−PVP and PVDF-$NaPF_6$ films. These observed changes in the SPE-2, PVDF−PVP, and PVDF−$NaPF_6$ films suggest that the C−F moiety of the PVDF polymer host may have had a significant role in dissolving both $NaPF_6$ and PVP. The Raman spectral profile of pure PVP showed several CH_2 vibration peaks in the range 607−1432 cm^{-1}; also, a characteristic peak at 1232 cm^{-1} that can be attributed to the N−C stretching for the carbonyl group was found.[64] Importantly, this peak disappeared in the Raman profile of SPE-2, indicating that the N−C moiety attached to the carbonyl group was involved in potential interaction with the PVDF polymer host and the Na salt.

Thermogravimetric analysis (TGA) was conducted in air for the PVDF powder, PDVF−$NaPF_6$ film, and SPE-2 to further understand the SPE-2 composition (Figure 9). The TGA profile of the PVDF powder showed thermal stability up to 400 °C. The first degradation starts after 400 °C, and one set of mass loss was

https://doi.org/10.1021/acsaem.2c01296
ACS Appl. Energy Mater. 2022, 5, 8812−8822

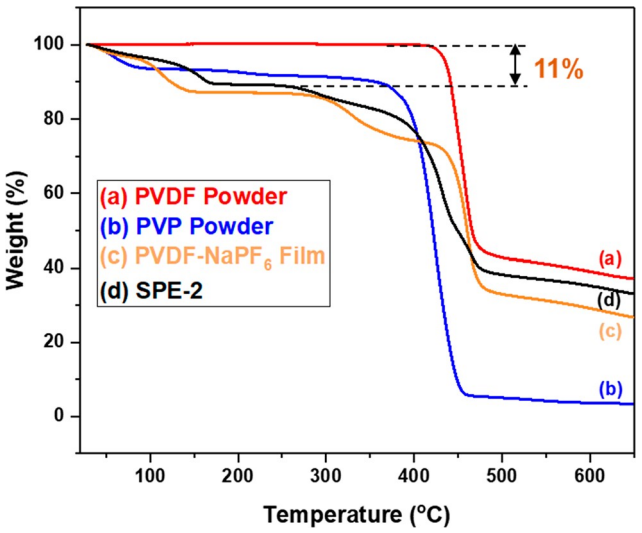

Figure 9. TGA profiles of (a) PVDF and (b) PVP powders, (c) PVDF–$NaPF_6$ film, and (d) SPE-2.

observed. In the thermogram of pure PVP, the distinct initial weight loss before 100 °C was due to the desorption of adsorbed water. Between 350 and 465 °C, another significant weight loss was observed, which could be attributed to the breakdown of the side groups (pyrrolidone) of PVP; the side groups were released and oxidized immediately.[65] Four sets of mass losses were observed from the PVDF–$NaPF_6$ film. The first two mass losses could be attributed to the release of adsorbed moisture and the evaporation of trapped DMF solvent inside the PVDF–$NaPF_6$ matrix. The third weight loss that started at 280 °C was due to the burning of $NaPF_6$ salt. Finally, the fourth thermal change exhibited at temperatures between 415 and 500 °C suggested that the decomposition of PVDF in the film ended with hydrogen fluoride formation. The TGA results of SPE-2 demonstrated the presence of 11% trapped DMF. It is believed that in the composite SPE-2 matrix, the trapped DMF solvent worked as a plasticizer and helped to increase the ionic conductivity.[18] Two more thermal changes in temperature ranges of 250–370 °C and 376–500 °C for the SPE-2 matrix may be associated with $NaPF_6$ burning, pyrrolidone side chain oxidation from PVP, and PVDF decomposition.[18]

Symmetric Cell Performance of SPE-2. To identify the chemical and electrochemical stability of SPE-2 against Na metal, we evaluated the interfacial resistance between SPE-2 and Na metal by EIS. The Na|SPE-2|Na symmetric cell showed very high interfacial resistance of about 0.95×10^8 Ω cm at room temperature (Figure S4). We constructed a symmetrical cell with a liquid electrolyte (Na|20 μL of 1 M $NaClO_4$ in EC/PC (1:1) + glass fiber + 20 μL of 1 M $NaClO_4$ in EC/PC (1:1)|Na) and characterized its impedance by EIS (Figure S5). Compared to the pure SPE-2 based symmetric cell, the liquid electrolyte-based symmetric cell exhibited lower interfacial resistance of 1.62×10^3 Ω cm with Na. Thus, steps were taken to reduce the interfacial resistance between the polymer and Na foil. Carbon cloth (0.1 mm, Fuel Cell Store) and 20 μL of liquid electrolytes (1 M $NaClO_4$ in EC/PC, 1:1) were introduced in the hybrid symmetric cell as presented in Figure 2. The carbon cloth minimized the side reactions, and 1 M liquid electrolyte decreased the interfacial resistance between Na and the SPE-2. Therefore, our hybrid symmetric cell exhibited reduced interfacial resistance of 1.31×10^3 Ω cm (Figure S6) compared to that of liquid and pure SPE-2 based symmetric cells.

Galvanostatic cycling with a series of constant areal current densities (e.g., 0.5, 1, 5, 8, and 10 mA cm^{-2}) was applied to the hybrid symmetric cell to evaluate the electrochemical stability of SPE-2 against Na metal (Figures 10a–e). The polarity of current for the galvanostatic experiments was switched every 10 min for 0.5, 1, and 10 mA cm^{-2} and every 60 min for 5 and 8 mA cm^{-2}. The galvanostatic cycling profiles highlight the compatibility and electrochemical stability of SPE-2 against Na metal. Particularly at 8 mA cm^{-2}, SPE-2 exhibited excellent stability for more than 800 h (see Figure 10e). For all galvanostatic cycling profiles (Figure 10a–e), increased current density (0.5 to 10 mA cm^{-2}) generated voltages higher than the expected values (Table S5). These observed extra voltages during the galvanostatic cycles are associated with the overpotential developed due to Na ion reduction and oxidation and Na ion transport through the electrode/electrolyte interphase or solid electrolyte and liquid electrolyte interfaces.[66] The resistance associated with the interfacial charge transfer gradually increased with increased current densities. The increase might be associated with the decreased interfacial contact between Na metal and SPE-2 that resulted in increased area specific resistance (ASR). The calculation of areal specific resistance can be found in the Supporting Information (Table S6). At 10 mA cm^{-2}, the ASR was 35 Ω cm^2, and the thickness of Na metal was only 15.01 μm. The amount of sodium that was plated on either side of the pellet can be estimated using Faraday's law (eq 3).

$$m = \frac{ItM}{nF} \tag{3}$$

where m is the mass of plated/stripped Na, F is the Faraday constant, M is the molar mass of Na, n is the valency of Na, which is one, I is the amount of current, and t is the duration of Na plating–stripping. The amount of Na that is stripped and consequently deposited in 10 min at 10 mA cm^{-2} is 1.12 mg. Moreover, to investigate the influence of added liquid electrolyte in the hybrid symmetric cell, a liquid electrolyte only based symmetric cell (Na|20 μL of 1 M $NaClO_4$ in EC/PC (1:1) + glass fiber + 20 μL of 1 M $NaClO_4$ in EC/PC (1:1)|Na) was assembled and used for galvanostatic cycling performance (Figure S8). Importantly, the critical current density for the liquid electrolyte based symmetric cell was just 2 mA cm^{-2} for less than 10 h, whereas the hybrid symmetric cell showed good Na plating–stripping performance at up to 10 mA cm^{-2} for more than 30 h. These findings strongly suggest that to achieve good electrochemical stability and for Na plating–stripping performance, the SPE-2 played an ample role in the hybrid symmetric cell system. The influence of different liquid organic solvents was also investigated. Instead of the EC/PC (1:1) solvent system, propylene carbonate (PC) and fluoroethylene carbonate (FEC) were introduced in a similar type of hybrid symmetric cell (Na foil + 20 μL of 1 M $NaClO_4$ in PC/FEC (95:5) + carbon cloth|SPE-2|carbon cloth + 20 μL of 1 M $NaClO_4$ in PC/FEC (95:5)|Na foil) for galvanostatic cyclic performance (Figure S7). This experiment was conducted to investigate the influence of PC and FEC on the compatibility between SPE-2 and Na metal. Notably, the PC/FEC mixed solvent system did not result in better performance than the EC/PC organic mixed solvent system.

Electrochemical Performance of Full Cell. A full cell (Na foil + 20 μL of 1 M $NaClO_4$ in EC/PC (1:1) + carbon cloth|SPE-

https://doi.org/10.1021/acsaem.2c01296
ACS Appl. Energy Mater. 2022, 5, 8812–8822

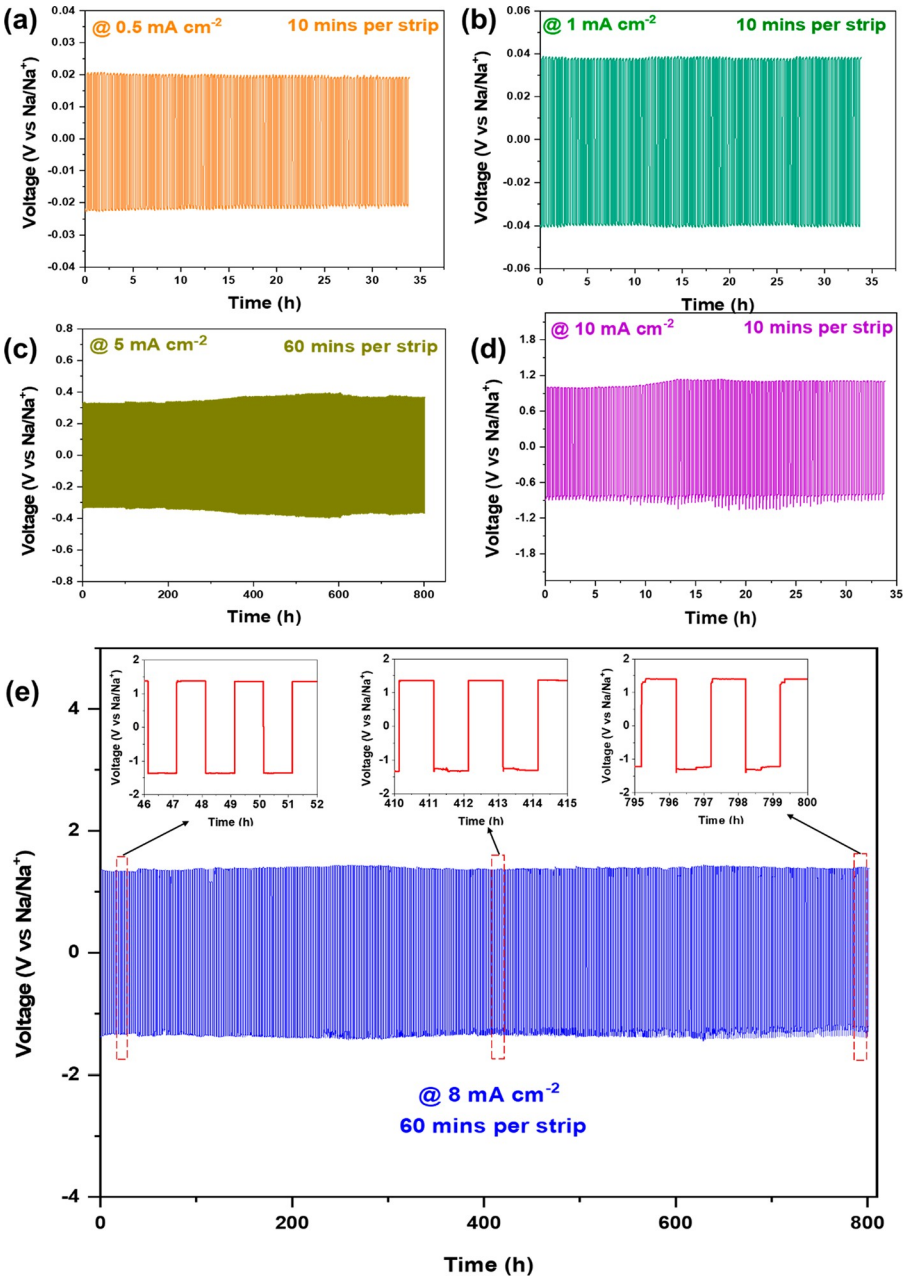

Figure 10. Galvanostatic cycling profiles of hybrid symmetrical cells (Na foil|20 μL of 1 M $NaClO_4$ in EC/PC (1:1) + carbon cloth|SPE-2|carbon cloth + 20 μL of 1 M $NaClO_4$ in EC/PC (1:1)|Na foil) (a) at 0.5 mA cm^{-2} for 100 cycles, (b) at 1 mA cm^{-2} for 100 cycles, (c) at 5 mA cm^{-2} for 400 cycles, (d) at 10 mA cm^{-2} for 100 cycles, and (e) at 8 mA cm^{-2} for 400 cycles.

2|20 μL of 1 M $NaClO_4$ in EC/PC (1:1)|NVP cathode) consisting of Na anode, NPV cathode, carbon cloth, SPE-2, and 1 M liquid electrolyte was constructed in a CR2032 coin cell case to demonstrate the application of SPE-2. Figure 11a shows the three charge−discharge curves (1, 30, and 60 cycles) of the full cell within a voltage range of 2−4 V vs Na at 0.1 C. A plateau in the charge profile at a voltage of 3.4 V vs Na is due to the oxidation of $Na_3V_2^{(III)}(PO_4)_3$ to $NaV_2^{(IV)}(PO_4)_3$.[18,67,68] The battery delivered a maximum of 105.5 mAh g^{-1} specific capacity. At the same C rate, a discharge plateau at 3.3 V for the first cycle was observed at a discharge capacity of 93.20 mAh g^{-1}. The discharge plateau can be attributed to the reduction of $NaV_2^{(IV)}(PO_4)_3$[18,68−70]

$$Na_3V_2(PO_4)_3 \rightleftharpoons 2Na^+ + 2e^- + NaV_2(PO_4)_3 \quad (4)$$

A specific capacity loss of 12.25 mAh g^{-1} was observed in the first cycle at 0.1 C; the loss may be attributed to the sluggish Na ion kinetics.[18] The observed potential polarization value (ΔE_p = 0.1 V) was lower than our previously reported research work.[18] After 100 consecutive charge−discharge cycles at 0.5C rate for the full cell, the NVP electrode shows an outstanding cycling performance with 86% capacity retention (Figure 11b). The Coulombic efficiency of the cell showed an average value of more than 99%, suggesting stable performance of the SPE-2 with the NVP electrode. For the first 10 cycles, however, the Coulombic efficiency was relatively low, which could be due to an unstable solid electrolyte interface (SEI) formation on the Na surface.[45] We propose that a portion of added liquid electrolyte in the cell was consumed, building an effective SEI on the Na surface and improving the electrochemical performance.[71]

https://doi.org/10.1021/acsaem.2c01296
ACS Appl. Energy Mater. 2022, 5, 8812−8822

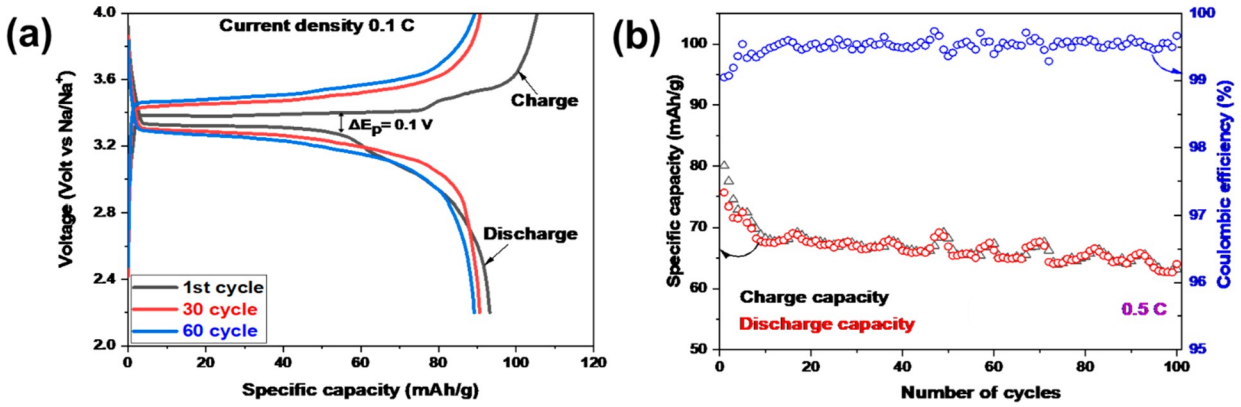

Figure 11. (a) Charge−discharge profile of the full cell at 0.1 C. (b) Cycling performance of the full cell at 0.5 C for 100 cycles.

CONCLUSIONS

We successfully fabricated a high Na ion conductive, filler-less composite solid polymer electrolyte based on a PVDF polymer host, PVP polymer binder, and $NaPF_6$ salt through a facile solution-casting process. Optimum composition of PVDF host polymer and $NaPF_6$ salt was identified (PVDF/$NaPF_6$ (9:1 molar ratio) and 11 wt % PVP in the total PVP and PVDF weight). The effects of $NaPF_6$ salt concentration and PVP binder in the presence or absence of SiO_2 nanofiller on Na ion conductivity were investigated by EIS. We believe that the PVP binder in the PVDF-based composite system played a crucial role in achieving fast Na ion conductivity and excellent Na plating−stripping performance. Based on our knowledge, this is the first study in which the PVP binder effect has been identified for the development of SPEs for ss-SIBs. A comprehensive characterization, including XRD, FTIR, Raman, and TGA, was conducted on the optimized SPE (SPE-2). SPE-2 had ionic conductivity of 8.51×10^{-4} S cm^{-1} and 8.36×10^{-3} S cm^{-1} at 23 and 83 °C, respectively. The low E_a value (0.19 eV) of the SPE-2 indicates fast ion transport in the composite environment through an ion-hopping mechanism. A hybrid symmetric cell (Na foil|20 μL of 1 M $NaClO_4$ in EC/PC + carbon cloth|SPE-2|carbon cloth + 20 μL of 1 M $NaClO_4$ in EC/PC|Na foil) using the SPE with the best composition exhibited excellent Na plating and stripping performance. SPE-2 exhibited low area specific resistance and was electrochemically stable with Na-metal electrodes up to 10 mA cm^{-2} for 100 cycles. A full cell consisting of SPE-2, Na anode, and NVP cathode showed a good discharge capacity of 93.20 mAh g^{-1} at 0.1 C. Good cycling performance was observed with 86% capacity retention from its initial value after 100 cycles. Excellent Coulombic efficiency (99%) indicated stable performance of SPE-2 with the NVP electrode. Overall, the findings highlight the promising applicability of SPEs in next-generation and environmentally friendly ss-SIB technology.

ASSOCIATED CONTENT

Supporting Information

The Supporting Information is available free of charge at https://pubs.acs.org/doi/10.1021/acsaem.2c01296.

FTIR spectral information on PVDF film, Raman spectral information on PVDF powder, SEM surface images of SPE-1, SPE-2, and SPE-3, EIS profiles of SPE-1, SPE-3, and three different symmetric cells, ionic conductivity containing tabular data of SPE-1−3, galvanostatic cycling profile of symmetric cell with SPE-2, observed and expected voltages for galvanostatic cycling profiles of full cell, charge−discharge profile of the full cell at different C-rates, and calculation of area specific resistance (ASR) (PDF)

AUTHOR INFORMATION

Corresponding Author

Venkataraman Thangadurai − *Department of Chemistry, University of Calgary, Calgary, Alberta T2N 1N4, Canada;* orcid.org/0000-0001-6256-6307; Email: vthangad@ucalgary.ca

Authors

Afshana Afroj Bristi − *Department of Chemistry, University of Calgary, Calgary, Alberta T2N 1N4, Canada*

Alfred Junio Samson − *Department of Chemistry, University of Calgary, Calgary, Alberta T2N 1N4, Canada*

Abinaya Sivakumaran − *Department of Chemistry, University of Calgary, Calgary, Alberta T2N 1N4, Canada*

Shantel Butler − *Geometric Energy Corporation, Calgary, Alberta T2P 3N9, Canada*

Complete contact information is available at: https://pubs.acs.org/10.1021/acsaem.2c01296

Author Contributions

Conceptualization: V.T. Methodology: A.A.B. and A.J.S. First draft preparation: A.A.B. Data collection and experiment: A.A.B. Investigation and data curation: A.A.B., A.J.S., and V.T. Validation: A.A.B. and A.J.S. Resources: V.T. Draft review and editing: A.A.B., A.J.S., A.S., S.B., and V.T. Supervision: V.T. Project administration and funding acquisition: S.B. and V.T.

Notes

The authors declare no competing financial interest.

ACKNOWLEDGMENTS

This work was funded by the Natural Sciences and Engineering Research Council of Canada (NSERC) Collaborative Research and Development (CRD) Grants and Geometric Energy Corporation, Calgary.

REFERENCES

(1) Devi, C.; Gellanki, J.; Pettersson, H.; Kumar, S. High Sodium Ionic Conductivity in PEO/PVP Solid Polymer Electrolytes with InAs Nanowire Fillers. *Sci. Rep.* **2021**, *11* (1), 1−8.

(2) Hasa, I.; Mariyappan, S.; Saurel, D.; Adelhelm, P.; Koposov, A. Y.; Masquelier, C.; Croguennec, L.; Casas-Cabanas, M. Challenges of

Today for Na-Based Batteries of the Future: From Materials to Cell Metrics. *J. Power Sources* **2021**, *482*, 228872.
(3) Fichtner, M.; Edström, K.; Ayerbe, E.; Berecibar, M.; Bhowmik, A.; Castelli, I. E.; Clark, S.; Dominko, R.; Erakca, M.; Franco, A. A.; Grimaud, A.; Horstmann, B.; Latz, A.; Lorrmann, H.; Meeus, M.; Narayan, R.; Pammer, F.; Ruhland, J.; Stein, H.; Vegge, T.; Weil, M. Rechargeable Batteries of the Future—The State of the Art from a BATTERY 2030+ Perspective. *Adv. Energy Mater.* **2021**, 2102904.
(4) Zhao, Q.; Liu, X.; Stalin, S.; Khan, K.; Archer, L. A. Solid-State Polymer Electrolytes with in-Built Fast Interfacial Transport for Secondary Lithium Batteries. *Nat. Energy* **2019**, *4* (5), 365−373.
(5) Vaalma, C.; Buchholz, D.; Weil, M.; Passerini, S. A Cost and Resource Analysis of Sodium-Ion Batteries. *Nat. Rev. Mater.* **2018**, *3*, 18013.
(6) Li, M.; Lu, J.; Chen, Z.; Amine, K. 30 Years of Lithium-Ion Batteries. *Adv. Mater.* **2018**, *30*, 1800561.
(7) Li, P.; Dong, X.; Li, C.; Liu, J.; Liu, Y.; Feng, W.; Wang, C.; Wang, Y.; Xia, Y. Anchoring an Artificial Solid−Electrolyte Interphase Layer on a 3D Current Collector for High-Performance Lithium Anodes. *Angew. Chemie - Int. Ed.* **2019**, *58* (7), 2093−2097.
(8) Liu, K.; Liu, Y.; Lin, D.; Pei, A.; Cui, Y. Materials for Lithium-Ion Battery Safety. *Sci. Adv.* **2018**, *4* (6), No. eaas9820.
(9) Zhao, W.; Yi, J.; He, P.; Zhou, H. Solid-State Electrolytes for Lithium-Ion Batteries: Fundamentals, Challenges and Perspectives. *Electrochem. Energy Rev.* **2019**, *2* (4), 574−605.
(10) Zhu, Z.; Hong, M.; Guo, D.; Shi, J.; Tao, Z.; Chen, J. All-Solid-State Lithium Organic Battery with Composite Polymer Electrolyte and Pillar[5]Quinone Cathode. *J. Am. Chem. Soc.* **2014**, *136* (47), 16461−16464.
(11) Yang, P.; Liu, L.; Li, L.; Hou, J.; Xu, Y.; Ren, X.; An, M.; Li, N. Gel Polymer Electrolyte Based on Polyvinylidenefluoride-Co- Hexafluoropropylene and Ionic Liquid for Lithium Ion Battery. *Electrochim. Acta* **2014**, *115*, 454−460.
(12) Liu, G.; Sun, X.; Yu, X.; Weng, W.; Yang, J.; Zhou, D.; Xiao, R.; Chen, L.; Yao, X. Na10SnSb2S12: A Nanosized Air-Stable Solid Electrolyte for All-Solid-State Sodium Batteries. *Chem. Eng. J.* **2021**, *420* (P2), 127692.
(13) Wan, H.; Mwizerwa, J. P.; Han, F.; Weng, W.; Yang, J.; Wang, C.; Yao, X. Grain-Boundary-Resistance-Less Na3SbS4-XSex Solid Electrolytes for All-Solid-State Sodium Batteries. *Nano Energy* **2019**, *66*, 104109.
(14) Wan, H.; Weng, W.; Han, F.; Cai, L.; Wang, C.; Yao, X. Bio-Inspired Nanoscaled Electronic/Ionic Conduction Networks for Room-Temperature All-Solid-State Sodium-Sulfur Battery. *Nano Today* **2020**, *33*, 100860.
(15) Zhang, Z.; Shao, Y.; Lotsch, B.; Hu, Y. S.; Li, H.; Janek, J.; Nazar, L. F.; Nan, C. W.; Maier, J.; Armand, M.; Chen, L. New Horizons for Inorganic Solid State Ion Conductors. *Energy Environ. Sci.* **2018**, *11* (8), 1945−1976.
(16) Zhao, C.; Liu, L.; Qi, X.; Lu, Y.; Wu, F.; Zhao, J.; Yu, Y.; Hu, Y. S.; Chen, L. Solid-State Sodium Batteries. *Adv. Energy Mater.* **2018**, *8*, 1703012.
(17) Abouali, S.; Yim, C. H.; Merati, A.; Abu-Lebdeh, Y.; Thangadurai, V. Garnet-Based Solid-State Li Batteries: From Materials Design to Battery Architecture. *ACS Energy Lett.* **2021**, *6* (5), 1920−1941.
(18) Bag, S.; Zhou, C.; Reid, S.; Butler, S.; Thangadurai, V. Electrochemical Studies on Symmetric Solid-State Na-Ion Full Cell Using Na3V2(PO4)3 Electrodes and Polymer Composite Electrolyte. *J. Power Sources* **2020**, *454*, 227954.
(19) Shen, L.; Deng, S.; Jiang, R.; Liu, G.; Yang, J.; Yao, X. Flexible Composite Solid Electrolyte with 80 Wt% Na3.4Zr1.9Zn0.1Si2.2-P0.8O12 for Solid-State Sodium Batteries. *Energy Storage Mater.* **2022**, *46*, 175−181.
(20) Li, N.-W.; Yin, Y.-X.; Yang, C.-P.; Guo, Y.-G. An Artificial Solid Electrolyte Interphase Layer for Stable Lithium Metal Anodes. *Adv. Mater.* **2016**, *28*, 1853−1858.
(21) Han, L.; Lehmann, M. L.; Zhu, J.; Liu, T.; Zhou, Z.; Tang, X.; Heish, C. Te; Sokolov, A. P.; Cao, P.; Chen, X. C.; Saito, T. Recent Developments and Challenges in Hybrid Solid Electrolytes for Lithium-Ion Batteries. *Front. Energy Res.* **2020**, *8*, 202.
(22) Popovic, J.; Brandell, D.; Ohno, S.; Hatzell, K. B.; Zheng, J.; Hu, Y. Y. Polymer-Based Hybrid Battery Electrolytes: Theoretical Insights, Recent Advances and Challenges. *J. Mater. Chem. A* **2021**, *9* (10), 6050−6069.
(23) Zhao, C.; Sun, Q.; Luo, J.; Liang, J.; Liu, Y.; Zhang, L.; Wang, J.; Deng, S.; Lin, X.; Yang, X.; Huang, H.; Zhao, S.; Zhang, L.; Lu, S.; Sun, X. 3D Porous Garnet/Gel Polymer Hybrid Electrolyte for Safe Solid-State Li-O2Batteries with Long Lifetimes. *Chem. Mater.* **2020**, *32* (23), 10113−10119.
(24) Lopez, J.; Mackanic, D. G.; Cui, Y.; Bao, Z. Designing Polymers for Advanced Battery Chemistries. *Nat. Rev. Mater.* **2019**, *4* (5), 312−330.
(25) Zhang, C.; Gamble, S.; Ainsworth, D.; Slawin, A. M. Z.; Andreev, Y. G.; Bruce, P. G. Alkali Metal Crystalline Polymer Electrolytes. *Nat. Mater.* **2009**, *8* (7), 580−584.
(26) Yamada, Y.; Wang, J.; Ko, S.; Watanabe, E.; Yamada, A. Advances and Issues in Developing Salt-Concentrated Battery Electrolytes. *Nat. Energy* **2019**, *4* (4), 269−280.
(27) St-Onge, V.; Cui, M.; Rochon, S.; Daigle, J.-C.; Claverie, J. P. Reducing Crystallinity in Solid Polymer Electrolytes for Lithium-Metal Batteries via Statistical Copolymerization. *Commun. Mater.* **2021**, *2* (1), 1−11.
(28) Pitawala, H. M. J. C.; Dissanayake, M. A. K. L.; Seneviratne, V. A. Combined Effect of Al2O3 Nano-Fillers and EC Plasticizer on Ionic Conductivity Enhancement in the Solid Polymer Electrolyte (PEO)-9LiTf. *Solid State Ionics* **2007**, *178* (13−14), 885−888.
(29) Du, Z.; Chen, X. C.; Sahore, R.; Wu, X.; Li, J.; Dudney, N. J. Effects of Plasticizer Content and Ceramic Addition on Electrochemical Properties of Cross-Linked Polymer Electrolyte. *J. Electrochem. Soc.* **2021**, *168* (5), 050549.
(30) Yin, H.; Han, C.; Liu, Q.; Wu, F.; Zhang, F.; Tang, Y. Recent Advances and Perspectives on the Polymer Electrolytes for Sodium/Potassium-Ion Batteries. *Small* **2021**, *17* (31), 2006627.
(31) Shan, Y.; Li, L.; Yang, X. Solid-State Polymer Electrolyte Solves the Transfer of Lithium Ions between the Solid-Solid Interface of the Electrode and the Electrolyte in Lithium-Sulfur and Lithium-Ion Batteries. *ACS Appl. Energy Mater.* **2021**, *4*, 5101.
(32) Abraham, K. M.; Jiang, Z.; Carroll, B. Highly Conductive PEO-like Polymer Electrolytes. *Chem. Mater.* **1997**, *9* (9), 1978−1988.
(33) Wu, J.; Yuan, L.; Zhang, W.; Li, Z.; Xie, X.; Huang, Y. Reducing the Thickness of Solid-State Electrolyte Membranes for High-Energy Lithium Batteries. *Energy Environ. Sci.* **2021**, *14* (1), 12−36.
(34) Jouault, N.; Zhao, D.; Kumar, S. K. Role of Casting Solvent on Nanoparticle Dispersion in Polymer Nanocomposites. *Macromolecules* **2014**, *47* (15), 5246−5255.
(35) Sun, Y.; Zhan, X.; Hu, J.; Wang, Y.; Gao, S.; Shen, Y.; Cheng, Y. T. Improving Ionic Conductivity with Bimodal-Sized Li 7 La 3 Zr 2 O 12 Fillers for Composite Polymer Electrolytes. *ACS Appl. Mater. Interfaces* **2019**, *11* (13), 12467−12475.
(36) Hema, M.; Tamilselvi, P. Lithium Ion Conducting PVA:PVdF Polymer Electrolytes Doped with Nano SiO2 and TiO2 Filler. *J. Phys. Chem. Solids* **2016**, *96*−*97*, 42−48.
(37) Molinari, N.; Mailoa, J. P.; Kozinsky, B. Effect of Salt Concentration on Ion Clustering and Transport in Polymer Solid Electrolytes: A Molecular Dynamics Study of PEO-LiTFSI. *Chem. Mater.* **2018**, *30* (18), 6298−6306.
(38) Wieczorek, W.; Raducha, D.; Zalewska, A.; Stevens, J. R. Effect of Salt Concentration on the Conductivity of PEO-Based Composite Polymeric Electrolytes. *J. Phys. Chem. B* **1998**, *102* (44), 8725−8731.
(39) Zhao, Y. M.; Yue, F. S.; Li, S. C.; Zhang, Y.; Tian, Z. R.; Xu, Q.; Xin, S.; Guo, Y. G. Advances of Polymer Binders for Silicon-Based Anodes in High Energy Density Lithium-Ion Batteries. *InfoMat* **2021**, *3* (5), 460−501.
(40) Munaoka, T.; Yan, X.; Lopez, J.; To, J. W. F.; Park, J.; Tok, J. B. H.; Cui, Y.; Bao, Z. Ionically Conductive Self-Healing Binder for Low Cost Si Microparticles Anodes in Li-Ion Batteries. *Adv. Energy Mater.* **2018**, *8*, 1703138.

https://doi.org/10.1021/acsaem.2c01296
ACS Appl. Energy Mater. 2022, 5, 8812−8822

(41) Zheng, M.; Wang, C.; Xu, Y.; Li, K.; Liu, D. A Water-Soluble Binary Conductive Binder for Si Anode Lithium Ion Battery. *Electrochim. Acta* **2019**, *305*, 555−562.
(42) Koczkur, K. M.; Mourdikoudis, S.; Polavarapu, L.; Skrabalak, S. E. Polyvinylpyrrolidone (PVP) in Nanoparticle Synthesis. *Dalt. Trans.* **2015**, *44* (41), 17883−17905.
(43) Gaur, M. S.; Indolia, A. P.; Rogachev, A. A.; Rahachou, A. V. Influence of SiO2 Nanoparticles on Morphological, Thermal, and Dielectric Properties of PVDF. *J. Therm. Anal. Calorim.* **2015**, *122* (3), 1403−1416.
(44) Singh, P.; Saroj, A. L. Effect of SiO2 Nano-Particles on Plasticized Polymer Blend Electrolytes: Vibrational, Thermal, and Ionic Conductivity Study. *Polym.-Plastics Technol. Mater.* **2021**, *60* (3), 298−305.
(45) Narayanan, S.; Reid, S.; Butler, S.; Thangadurai, V. Sintering Temperature, Excess Sodium, and Phosphorous Dependencies on Morphology and Ionic Conductivity of NASICON Na3Zr2Si2PO12. *Solid State Ionics* **2019**, *331*, 22−29.
(46) Shen, Z.; Cheng, Y.; Sun, S.; Ke, X.; Liu, L.; Shi, Z. The Critical Role of Inorganic Nanofillers in Solid Polymer Composite Electrolyte for Li+ Transportation. *Carbon Energy* **2021**, *3* (3), 482−508.
(47) Borkowska, R.; Reda, A.; Zalewska, A.; Wieczorek, W. Composite Polyether Electrolytes with Lewis Acid Type Additives. *Electrochim. Acta* **2001**, *46* (10−11), 1737−1746.
(48) Barbosa, J. C.; Correia, D. M.; Fernández, E. M.; Fidalgo-Marijuan, A.; Barandika, G.; Gonçalves, R.; Ferdov, S.; De Zea Bermudez, V.; Costa, C. M.; Lanceros-Mendez, S. High-Performance Room Temperature Lithium-Ion Battery Solid Polymer Electrolytes Based on Poly(Vinylidene Fluoride- Co-Hexafluoropropylene) Combining Ionic Liquid and Zeolite. *ACS Appl. Mater. Interfaces* **2021**, *13* (41), 48889−48900.
(49) Bag, S.; Zhou, C.; Kim, P. J.; Pol, V. G.; Thangadurai, V. LiF Modified Stable Flexible PVDF-Garnet Hybrid Electrolyte for High Performance All-Solid-State Li−S Batteries. *Energy Storage Mater.* **2020**, *24*, 198−207.
(50) Aziz, S. B.; Woo, T. J.; Kadir, M. F. Z.; Ahmed, H. M. A Conceptual Review on Polymer Electrolytes and Ion Transport Models. *J. Sci. Adv. Mater. Devices* **2018**, *3* (1), 1−17.
(51) Ponmani, S.; Prabhu, M. R. Development and Study of Solid Polymer Electrolytes Based on PVdF-HFP/PVAc: Mg (ClO4)2 for Mg Ion Batteries. *J. Mater. Sci. Mater. Electron.* **2018**, *29* (17), 15086−15096.
(52) Mishra, R.; Singh, S. K.; Gupta, H.; Tiwari, R. K.; Meghnani, D.; Patel, A.; Tiwari, A.; Tiwari, V. K.; Singh, R. K. Polar *β*-Phase PVdF-HFP-Based Freestanding and Flexible Gel Polymer Electrolyte for Better Cycling Stability in a Na Battery. *Energy Fuels* **2021**, *35* (18), 15153−15165.
(53) Cai, X.; Lei, T.; Sun, D.; Lin, L. A Critical Analysis of the *α*, *β* and *γ* Phases in Poly(Vinylidene Fluoride) Using FTIR. *RSC Adv.* **2017**, *7* (25), 15382−15389.
(54) Esterly, D. M.; Love, B. J. Phase Transformation to *β*-Poly(Vinylidene Fluoride) by Milling. *J. Polym. Sci., Part B: Polym. Phys.* **2004**, *42* (1), 91−97.
(55) Hasegawa, R.; Takahashi, Y.; Chatani, Y.; Tadokoro, H. Crystal Structures of Three Crystalline Forms of Poly(Vinylidene Fluoride). *Polym. J.* **1972**, *3* (5), 600−610.
(56) Okada, D.; Kaneko, H.; Kato, K.; Furumi, S.; Takeguchi, M.; Yamamoto, Y. Colloidal Crystallization and Ionic Liquid Induced Partial *β*-Phase Transformation of Poly(Vinylidene Fluoride) Nanoparticles. *Macromolecules* **2015**, *48* (8), 2570−2575.
(57) Wiegmann, J.; Leppin, C.; Langhoff, A.; Schwaderer, J.; Beuermann, S.; Johannsmann, D.; Weber, A. P. Influence of the Solvent Evaporation Rate on the *β*-Phase Content of Electrosprayed PVDF Particles and Films Studied by a Fast Multi-Overtone QCM. *Adv. Powder Technol.* **2022**, *33* (3), 103452.
(58) Martins, P.; Lopes, A. C.; Lanceros-Mendez, S. Electroactive Phases of Poly(Vinylidene Fluoride): Determination, Processing and Applications. *Prog. Polym. Sci.* **2014**, *39* (4), 683−706.
(59) Kumar, K. K.; Ravi, M.; Pavani, Y.; Bhavani, S.; Sharma, A. K.; Narasimha Rao, V. V. R. Investigations on PEO/PVP/NaBr Complexed Polymer Blend Electrolytes for Electrochemical Cell Applications. *J. Membr. Sci.* **2014**, *454*, 200−211.
(60) Kam, W.; Liew, C. W.; Lim, J. Y.; Ramesh, S. Electrical, Structural, and Thermal Studies of Antimony Trioxide-Doped Poly(Acrylic Acid)-Based Composite Polymer Electrolytes. *Ionics (Kiel).* **2014**, *20* (5), 665−674.
(61) Li, Y.; Xu, J. Z.; Zhu, L.; Xu, H.; Pan, M. W.; Zhong, G. J.; Li, Z. M. Multiple Stage Crystallization of Gamma Phase Poly(Vinylidene Fluoride) Induced by Ion-Dipole Interaction as Revealed by Time-Resolved FTIR and Two-Dimensional Correlation Analysis. *Polymer (Guildf).* **2014**, *55* (18), 4765−4775.
(62) Zhou, C.; Bag, S.; He, T.; Lv, B.; Thangadurai, V. A 20 °C Operating High Capacity Solid-State Li-S Battery with an Engineered Carbon Support Cathode Structure. *Appl. Mater. Today* **2020**, *19*, 100585.
(63) Heyns, A. M. The i. r. and Raman Spectra of Sodium Hexafluorophosphate NaPFs-Hz0. *Spectrochim. Acta* **1977**, *33*, 315−322.
(64) Fini, A.; Cavallari, C.; Ospitali, F. Raman and Thermal Analysis of Indomethacin/PVP Solid Dispersion Enteric Microparticles. *Eur. J. Pharm. Biopharm.* **2008**, *70* (1), 409−420.
(65) Szilágyi, I. M.; Santala, E.; Heikkilä, M.; Kemell, M.; Nikitin, T.; Khriachtchev, L.; Räsänen, M.; Ritala, M.; Leskelä, M. Thermal Study on Electrospun Polyvinylpyrrolidone/Ammonium Metatungstate Nanofibers: Optimising the Annealing Conditions for Obtaining WO3 Nanofibers. *J. Therm. Anal. Calorim.* **2011**, *105* (1), 73−81.
(66) Bieker, G.; Winter, M.; Bieker, P. Electrochemical in Situ Investigations of SEI and Dendrite Formation on the Lithium Metal Anode. *Phys. Chem. Chem. Phys.* **2015**, *17* (14), 8670−8679.
(67) Zeng, X.; Peng, J.; Guo, Y.; Zhu, H.; Huang, X. Research Progress on Na3V2(PO4)3 Cathode Material of Sodium Ion Battery. *Front. Chem.* **2020**, *8* (July), 1−15.
(68) Bag, S.; Murarka, H.; Zhou, C.; Bhattacharya, A.; Jokhakar, D.; Pol, V. G.; Thangadurai, V. Understanding the Na-Ion Storage Mechanism in Na3+ XV2- XMx(PO4)3(M = Ni2+, Co2+, Mg2+x = 0.1−0.5) Cathodes. *ACS Appl. Energy Mater.* **2020**, *3* (9), 8475−8486.
(69) Zhang, Y.; Zhao, H.; Du, Y. Symmetric Full Cells Assembled by Using Self-Supporting Na3V2(PO4)3 Bipolar Electrodes for Superior Sodium Energy Storage. *J. Mater. Chem. A* **2016**, *4* (19), 7155−7159.
(70) Jian, Z.; Sun, Y.; Ji, X. A New Low-Voltage Plateau of Na3V2(PO4)3 as an Anode for Na-Ion Batteries. *Chem. Commun.* **2015**, *51* (29), 6381−6383.
(71) Huang, Y.; Zhao, L.; Li, L.; Xie, M.; Wu, F.; Chen, R. Electrolytes and Electrolyte/Electrode Interfaces in Sodium-Ion Batteries: From Scientific Research to Practical Application. *Adv. Mater.* **2019**, *31*, 1808393.

https://doi.org/10.1021/acsaem.2c01296
ACS Appl. Energy Mater. 2022, 5, 8812−8822